PHOTONICS Research

Phosphor-free microLEDs with ultrafast and broadband features for visible light communications

ZHENHUAN TIAN,[1,2] QIANG LI,[1,2] XUZHENG WANG,[1,2] MINGYIN ZHANG,[1,2] XILIN SU,[1,2] YE ZHANG,[1,2] YUFENG LI,[1,2] FENG YUN,[1,2,*] AND S. W. RICKY LEE[3,4]

[1]Shaanxi Provincial Key Laboratory of Photonics & Information Technology, Xi'an Jiaotong University, Xi'an 710049, China
[2]Solid-State Lighting Engineering Research Center, Xi'an Jiaotong University, Xi'an 710049, China
[3]Department of Mechanical and Aerospace Engineering, The Hong Kong University of Science and Technology, Clear Water Bay, Kowloon, Hong Kong, China
[4]HKUST LED-FPD Technology R&D Center at Foshan, Foshan 528200, China
*Corresponding author: fyun2010@mail.xjtu.edu.cn

Received 28 October 2020; revised 15 December 2020; accepted 18 January 2021; posted 19 January 2021 (Doc. ID 413069); published 16 March 2021

Modulation bandwidth and the emission region are essential features for the widespread use of visible light communications (VLC). This paper addresses the contradictory requirements to achieve broadband and proposes ultrafast, asymmetric pyramids grown on adjacent deep concave holes via lateral overgrowth. Multicolor emission with an emission region between 420 nm and 600 nm is obtained by controlling the growth rate at different positions on the same face, which also can provide multiple subcarrier frequency points for the employment of wavelength division multiplexing technology. The spontaneous emission rate distinction is narrowed by lowering the number of the crystal plane, ensuring a high modulation bandwidth over broadband. More importantly, the residual stress and dislocation density were minimized by employing a patterned substrate, and lateral overgrowth resulted in a further enhancement of the recombination rate. Finally, the total modulation bandwidth of multiple subcarriers of the asymmetric pyramids is beyond GHz. These ultrafast, multicolor microLEDs are viable for application in VLC systems and may also enable applications for intelligent lighting and display.

https://doi.org/10.1364/PRJ.413069

1. INTRODUCTION

Over the last few years, visible light communications (VLC) based on white light-emitting diodes (LEDs) have received significant attention due to advantages such as fast reaction speed, low cost, freedom from electromagnetic interference, and high reliability [1–4]. The widespread use of a VLC system based on LEDs requires a simultaneous increase in the modulation bandwidth and emission region. Nevertheless, commercially available broad-area LEDs developed for lighting can only support modulation bandwidths within tens of MHz, which can barely meet today's rapidly increasing requirement for high-speed data transmission [5,6]. By shrinking the LED dimensions to microscale and growing these microLEDs on a semi/nonpolar GaN substrate, the modulation bandwidth can be significantly improved [7]. Unfortunately, semi/nonpolar wafers are complicated and expensive for commercial LEDs. As an alternative approach, the selective area growth (SAG) method was employed, in which micropyramid structures containing a semipolar facet can be easily obtained [8]. These microsized pyramids showed remarkably faster radiative recombination rates than the typical *c*-plane LEDs [7,9], since the internal polarization fields can be partially eliminated. However, these micropyramids structures lack a large enough color emission region, which is inapplicable for the integration of lighting and communications. Additionally, this monochromatic source cannot support the employment of wavelength division multiplexing (WDM) technology, which can significantly increase the total modulation bandwidth through the combination of individual subcarriers [10–12].

To produce broadband emission, the widely adopted approach is to use blue LEDs to excite some rare-earth phosphors. Although highly used, this approach is not suitable for a high-speed VLC system because the phosphors show a large fluorescent lifetime (~μs to ms) and low intrinsic bandwidth [13,14]. These phosphor-related problems also can be overcomefv through the SAG method, by which phosphor-free microLEDs can be obtained on specially designed two-dimensional (2D) patterned substrates. These microstructures, including the microstripes, microtrapezoidal structures, and a hexagonal annular structure, contain various crystal planes, on which different multiple quantum well (MQW) thicknesses and indium compositions are formed [15–17]. However, the employment of these multifacets, including polar, semipolar, and nonpolar facets, such as (0001), {11–22}, {10–12}, {10–1–x}, results in a variation of the carrier lifetime from several tens of ps to several hundred of ns [18,19]. It causes a nonuniform modulation bandwidth for different wavelengths, which reduces the data transfer rate. Even though a high modulation bandwidth can be guaranteed without multifacets such as pyramid structures, a large enough emission region can not be reached. In other words, there are contradictory requirements to achieve broadband emission and a high modulation bandwidth, which are both extremely important for VLC systems.

To solve this contradiction, a new strategy based on the SAG method was proposed to achieve phosphor-free microstructures. A closely connected deep-hole patterned substrate was employed in this strategy to replace the individual 2D pattern in the traditional SAG method. Lateral overgrowth appeared during the microstructure growth because of this double-hole pattern, contributing to the growth rate distinction and broadband feature of these microstructures. Instead of multifacets, this multicolor asymmetric pyramid structure only contains (0001) and {1–101} facets, for which the variation of the carrier lifetime is effectively narrowed by reducing the number of the facets. Moreover, the spontaneous emission rate can be further improved by this deep-hole pattern and lateral overgrowth, due to the reduced residual stress and dislocation density. As a result, a high modulation bandwidth over broadband can be easily achieved by using our strategy. The total modulation bandwidth of multiple subcarriers will be beyond GHz by using WDM technology afterward. These ultrafast and multicolor 3D microLEDs are suitable for application in a high-speed VLC system. This is also the first attempt, to the best of our knowledge, to achieve high-speed microLEDs based on the SAG method, which offers an excellent opportunity to enable many new applications through the integration of lighting, display, and communications [20].

2. EXPERIMENT

An asymmetric pyramid structure was fabricated using a combined process: the laser drilling method to obtain a 3D patterned sapphire substrate, and the SAG method to grow the pyramid structures. A double bowl-like concave pattern was obtained by the laser drilling method, as shown in Figs. 1(a) and 1(b). Then, 3D microstructures were grown above a pair of concave holes via the SAG method using metal organic vapor phase epitaxy (MOVPE). If the hole distance is small enough, a complete asymmetric pyramid, containing (0001) facet and {1–101} facet, will be obtained by the coalescence of the adjacent pyramids through the lateral overgrowth, as demonstrated in Figs. 1(d) and 1(e).

The morphology of the asymmetric pyramid was examined using the scanning electron microscope (GeminiSEM 500, Carl Zeiss Microscopy GmbH, Jena, Germany). High-angle annular dark-field scanning transmission electron microscopy

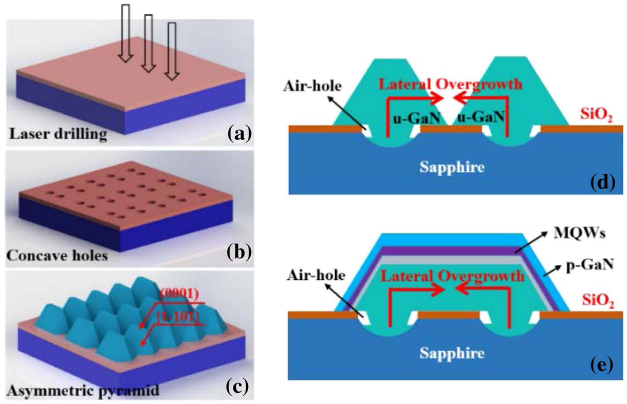

Fig. 1. Schematic illustrations of the fabrication process flow and lateral overgrowth for asymmetric pyramids.

(HAADF-STEM) (JEM-F200, JEOL Ltd., Tokyo) was used to inspect the cross-section of the MQWs. We performed a room temperature photoluminescence (PL) and micro-PL experiment combined with SEM to characterize the broadband emission, and used Raman spectroscopy and a low-temperature PL to examine the material quality and residual stress. To inspect the recombination rate, the time-resolved PL (TRPL) spectra (FLS980, Edinburgh Instruments, Livingston, UK) were measured with a picosecond pulsed diode laser (EPL Series, Edinburgh Instruments). The wavelength, linewidth, and repetition rate of the pulsed laser were 375 nm, 1.5 nm, and 20 MHz, respectively.

3. RESULTS AND DISCUSSION

A. Completely Merged Asymmetric Pyramids and Broadband Emission

The distance between the adjacent drilling holes must be carefully controlled to obtain completely merged asymmetric pyramids and broadband emission. Therefore, substrate patterns with hole distances L of 10 μm, 17 μm, 20 μm, and 25 μm were prepared, respectively, to get the optimal selection. Then, 3D microstructures were obtained with different substrate patterns under the same growth conditions.

Figure 2(a) shows the SEM and optical images of these 3D microstructures. Room temperature PL was also measured on samples 1–4, respectively, as shown in Fig. 2(b). From these figures, we can summarize that when the L is half of the lateral pitch size (sample 4, $L = 25$ μm), separated single pyramids are obtained. In that condition, the distance of the adjacent holes is too large to generate the coalescence of the adjacent pyramid. Coalescence appears by minimizing L, and eventually, the partially connected pyramids (sample 3, $L = 20$ μm) completely merge to asymmetric pyramids (sample 2, $L = 17$ μm). For samples 3 and 4, which were not completely merged samples, the (0001) facets of the adjacent pyramids have not been joined together before the end of the growth. Thus, no obvious wavelength distinction appears because there was not an enough growth rate and the indium (In) composition distinction on the (0001) facet [21]. Multiwavelength appears when the hole distance reaches 17 μm, by which a completely

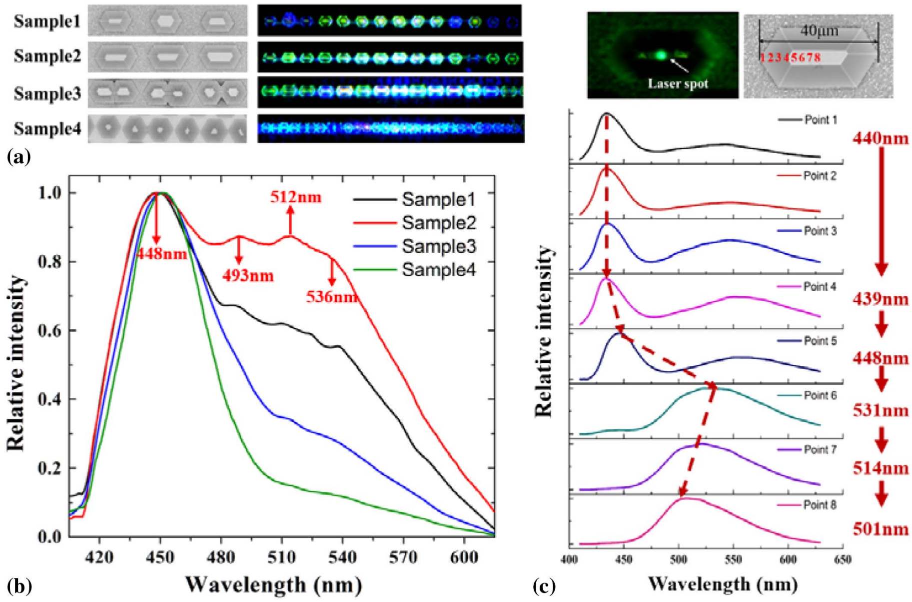

Fig. 2. (a) Optical images emitted by 405 nm laser and filtered by 450 nm filter; (b) PL intensity of samples 1, 2, 3, and 4; and (c) wavelength distribution for sample 2.

merged (0001) facet is obtained. Growth rate and In composition distinction show up on the (0001) facet through coalescence. With a continually decreasing distance, the vertical length of the asymmetric pyramids increases, accompanied by a reduction in the lateral length (sample 1, $L = 10$ μm). In this situation, the asymmetric pyramid is completely merged before the end of the growth. The (0001) facet will stack at a uniform growth rate after being completely merged. Thus, the variation of the wavelength is shrunk. Moreover, the In segregation is weakened due to the reduced lateral length and transverse diffusion distance. As a result, the wavelength range is narrowed by the reduced hole distance and lateral length of the asymmetric pyramids.

The results demonstrate that the hole distance is not only associated with the structure morphology but, more importantly, it also affects the emission region. To obtain a high data transfer rate and broadband emission, sample 2 with the largest emission region is the best choice. Therefore, sample 2 was selected to further develop the deep reason for broadband emission and the impact of lateral growth on the modulation bandwidth.

B. Structural Characteristics of Completely Merged Asymmetric Pyramid

To investigate the reason for the broadband emission of the completely merged asymmetric pyramid, micro-PL excitation was carried out to characterize the wavelength variation of sample 2, which showed the largest emission region. Light spectra of 8 points from the edge to the middle of sample 2 were measured by the micro-PL, as shown in Fig. 2(c). It can be found that the peak wavelengths of the first four points, located on the {10–11} facets, are all focused at a position of 440 nm, with 1 nm variation. The constant emission peak of semipolar facets is highly consistent with the previous study [22,23]. A large red shift appears from point 4 to point 5 due to the crystal plane switch. Compared to point 5, the last three points show a significantly large red shift, with a several nanometers blue shift from point 6 to point 8.

To further explain the reason for this wavelength variation, STEM was used to check the microstructure of the sample 2. Slices (80 nm thick) of the asymmetric pyramid along the centerline were fabricated by a focused ion beam (FIB). Figures 3(a)–3(d) show the HAADF-STEM images for the MQWs of different positions on this cross-section. Figure 3(e) is the SEM image of the cross-section of this asymmetric

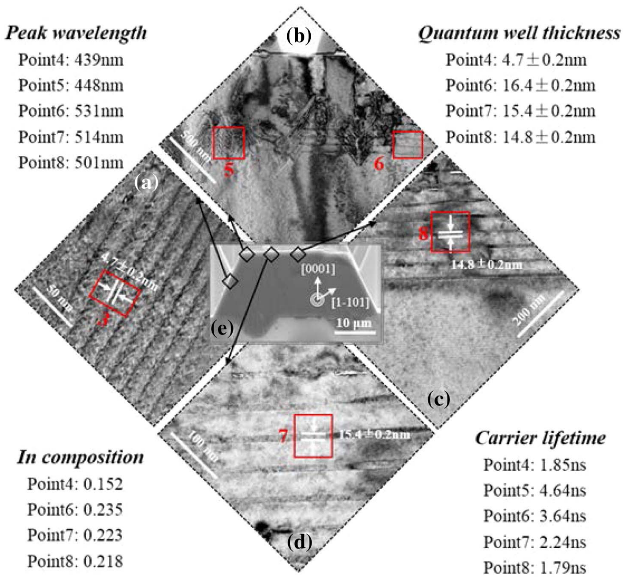

Fig. 3. Cross-section HAADF-STEM images of the point (a) at the semipolar facet, (b) at the edge of (0001) polar facet, (c) at the central part of (0001) facet, and (d) the area in between. The insert image (e) is the SEM image of the cross-section.

pyramid. We focused on four regions: the semipolar facet [Fig. 3(a)], the edge of (0001) polar facet [Fig. 3(b)], the lateral overgrowth edge of (0001) facet, and the area in between. The information of In composition and quantum well thickness for these positions can be measured from STEM images except for point 5, which contains a lot of V-shape defects. The In composition of points 4, 6, 7, and 8 can be extracted from the HAADF-STEM intensity ratio between In and Ga. Peak wavelength and carrier lifetime of these points are also listed in Fig. 3 to better analyze the relationship between these four parameters.

The wavelength, QW thickness, and In composition of point 4 and point 6 are 439 nm, 4.7 ± 0.2 nm, and 15.2%, and 531 nm, 16.4 ± 0.2 nm, and 23.5%, respectively. Point 6, located on the *c* plane, shows a relatively higher growth rate compared to the structure grown on the {10–11} facets, resulting in a larger width of MQWs. Additionally, the In composition on InGaN MQWs is much higher along the *c* axis. The band tilt of the MQWs and the charge separation in QWs on the {10–11} facets are also alleviated because of the weakened polarization on the semipolar facets [24]. All these factors lead to a wavelength distinction between point 4 and point 6. A slight decrease of the InGaN well thickness and In contents appears on the points from the edge to the middle of (0001) facet, indicating that the growth rate is not uniform along the *c* plane. The *c*-plane growth rate distinction derives from the species migrating, triggering a reduction of the thickness-enhancement ratio and In contents [25]. This growth rate distinction results in a blue shift of several nanometers from point 6 to point 8. Figure 3(b) also indicates that the crystal quality is poor on the edge of the cross-section with a lot of V-shaped defects. It is originated from the spatial discontinuity and tremendous growth rate difference at the junction of the semipolar and polar facets [16,26], leading to a wavelength separation between point 5 and other points on the *c* plane. These results demonstrate that the broadband emission is mainly due to the growth rate distinction on the (0001) facet, which is totally different from the previous study of phosphor-free microLEDs [15–17].

C. High-Modulation Bandwidth over a Broad Emission Region

Expect for the emission region, the spontaneous recombination of the asymmetric pyramid is also effectively enhanced. To characterize the carrier lifetime of the asymmetric pyramid, the temporal decay maps (TDMs) were recorded by measuring the PL intensity over a range of specific wavelengths as a function of decay time. Figures 4(a)–4(c) show the wavelength scanning of room temperature TRPL across a broad wavelength range from 430 nm to 540 nm for sample 2 (asymmetric pyramid), with sample 4 (single pyramid) and the planar LED as the references. The single pyramid has an emission spectrum mainly concentrated near 443 nm, along with a relatively weaker long-wavelength emission from (0001) facet. The emission spectrum for the planar LED is rather short, with only one peak emission at 454 nm. For comparison, the emission spectral range of the asymmetric pyramid structure, which ranges from 430 nm to 540 nm, is significantly broadened compared to the other two. More importantly, the decay tails of the asymmetric pyramid are significantly reduced in such a large

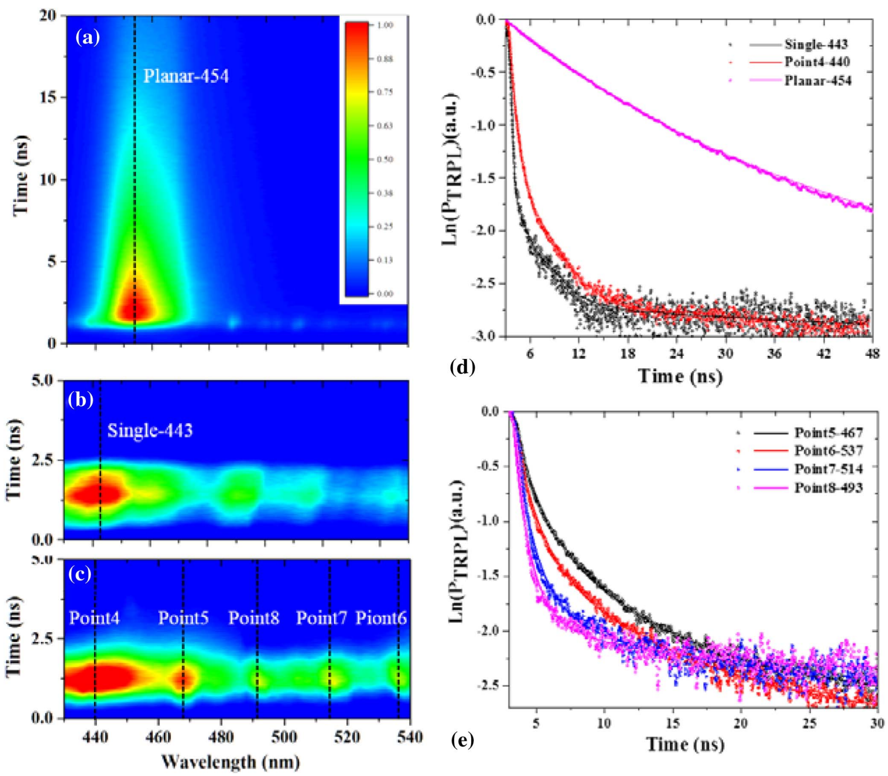

Fig. 4. Temporal decay maps of (a) planar LEDs, (b) a single pyramid, and (c) an asymmetric pyramid. TRPL decay curves measured at room temperature for (d) different samples at the main emission wavelength and (e) an asymmetric pyramid with several characteristic peaks.

emission range, indicating a great enhancement of the recombination rate.

To further investigate the lifetime and recombination rate of the carrier at different positions, the TRPL spectra of individual wavelengths are extracted from the TDMs and the normalized PL intensities are drawn on a natural logarithmic scale. Figure 4(d) shows the TRPL spectra of the planar LED, the single pyramid, and the asymmetric pyramid at the main emission wavelengths. Figure 4(e) is the TPRL spectra of the asymmetric pyramid with several characteristic peaks, corresponding to points 5, 6, 7, and 8 in Fig. 3.

The carrier lifetime τ, radiative-recombination carrier lifetime τ_r, and nonradiative recombination carrier lifetime τ_{nr}, can be calculated using [27]

$$\tau_{\mathrm{nr}} = 2\tau_{\mathrm{final}}, \qquad \tau_r = \frac{2\tau_{\mathrm{initial}} \cdot \tau_{\mathrm{final}}}{\tau_{\mathrm{final}} - \tau_{\mathrm{initial}}}, \tag{1}$$

where τ_{initial} and τ_{final} represent the lifetime at the initial and the final stage, respectively, which can be obtained from the slope on the curve of $\ln(P_{\mathrm{TRPL}})$ and t. The overall time constant τ is equal to

$$\tau = \frac{1}{\frac{1}{\tau_r} + \frac{1}{\tau_{\mathrm{nr}}}}. \tag{2}$$

The maximum 3 dB modulation bandwidth $f_{3\,\mathrm{dB}}$ can be written as

$$f_{3\,\mathrm{dB}} = \frac{\sqrt{3}}{2\pi\tau_{\mathrm{eff}}}, \tag{3}$$

where $\tau_{\mathrm{eff}} = \tau/2.5$ is the differential carrier lifetime [28,29].

Table 1 lists the calculated results of τ_{intal}, τ_{final}, τ_r, τ_{nr}, τ, and $f_{3\,\mathrm{dB}}$ for these characteristic peaks. For the different carrier frequency/characteristic peak, the corresponding carrier lifetime is different, resulting in a different modulation bandwidth. We define the modulation bandwidth for a specific point of the asymmetric pyramid as $f_{3\,\mathrm{dB}}^{\mathrm{point\_}i}$. The modulation bandwidth and data transfer rate obtained based on WDM technology can be quantitatively calculated. According to Shannon's theorems [30], the conventional channel capacity or the maximum data transfer rate is

$$D = \sum f_{3\,\mathrm{dB}}^{\mathrm{point\_}i} \cdot \log_2(1 + S_{\mathrm{point\_}i}/N_{\mathrm{point\_}i}), \tag{4}$$

where S and N are the signal variance and the noise variance.

The difference in noise variance is negligible for different emission wavelengths, while the difference in signal variance is nonignorable, but within an order of magnitude. To simplify this calculation, we just assume that either S or N is the same for each characteristic peak. Thus, Eq. (4) can be simplified as

$$D = \log_2(1 + S/N) \cdot \sum f_{3\,\mathrm{dB}}^{\mathrm{point\_}i}. \tag{5}$$

This formula means that the value of the total channel capacity is proportional to total modulation bandwidth $\sum f_{3\,\mathrm{dB}}^{\mathrm{point\_}i}$, which is the sum of the modulation bandwidth of these characteristic peaks.

The calculated modulation bandwidth of single pyramid and asymmetric pyramid MQWs on the semipolar facet (point 4) increased dozens of times compared to planar LED, due to the suppression of the quantum confinement stark effect (QCSE) of the semipolar facet. More importantly, the decay time of the asymmetric pyramid MQWs on a polar facet (points 6–8) also showed the similar or even better performance compared to that grown on the semipolar facets. Even point 5, at the junction of the polar facet and semipolar facet with plenty of V-shaped defects, still shows an enhancement of several times. The total modulation bandwidth of multiple subcarriers of the asymmetric pyramid is beyond GHz, which is almost a 100-times improvement compared to the planar LED. The results indicate that the asymmetric pyramid structure can provide a high recombination rate and modulation bandwidth over a broad emission region, contributing to a superior data transfer rate using WDM technology.

D. Stress Relief by Lateral Overgrowth to Improve the Spontaneous Emission Rate

Possible reasons that contribute to the reduction of the carrier lifetime and enhancement of the recombination rate are stress reduction and material quality improvement. To prove it, micro-Raman scattering measurements for an asymmetric pyramid (sample 1) were performed, with the planar LED as the reference. Points 6–8, which correspond to the lateral overgrowth (LO) window, wing, and edge, respectively, were tested. Figure 5 shows the Raman spectra of the E_2 (high) phonon, in which the peak and linewidth have been extensively used to quantify the stress and crystalline quality in GaN epilayers. The E_2 (high) linewidths of asymmetric pyramid LO wing, edge, window, and planar LED were observed at 2.17, 2.96, 2.77, and 3.15 cm^{-1}, respectively. The linewidth of the asymmetric pyramid is far less than that of the planar LED, indicating a dislocation density reduction. The minimum in the E_2 (high) phonon linewidth is visible in the LO wing region of the asymmetric pyramids. This illustrates that the decreased defect density is due to the lateral overgrowth, which agrees with the previous study [31,32]. The increased material quality obviously will contribute to the recombination rate enhancement.

Table 1. Decay Parameters for Single Pyramid, Planar LEDs, and Asymmetric Pyramid

Sample Name	τ_{initial} (ns)	τ_{final} (ns)	τ_r (ns)	τ_{nr} (ns)	τ (ns)	$f_{3\,\mathrm{dB}}^{\mathrm{point\_}i}$ (MHz)
Single–443	0.56	192.44	1.13	384.88	1.13	611.10
Planar–454	18.26	94.61	45.26	189.21	36.52	18.87
Point 4–440	0.92	299.16	1.85	598.33	1.85	373.28
Point 5–467	2.32	61.87	4.82	123.74	4.64	148.41
Point 6–537	1.82	70.38	3.73	140.75	3.64	189.46
Point 7–514	1.12	126.77	2.26	253.54	2.24	307.47
Point 8–493	0.90	209.06	1.80	418.12	1.79	384.72

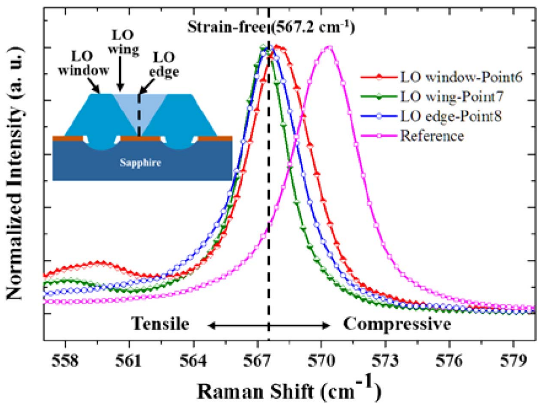

Fig. 5. Raman spectra recorded on the lateral overgrowth (LO) window, wing, and edge region, accompanied by a planar LED as a reference. The inset displays the recording of the spectra.

The E_2 (high) peak also was observed to examine the effectiveness of the strain relief for recombination rate enhancement. Referring back to the intrinsic value of 567.2 cm^{-1} [33] for stress-free GaN, the frequency shifts '$\Delta\omega$' were 0.22, 0.77, 0.33, and 3.09 cm^{-1}. The corresponding strain also can be estimated by [34]

$$\varepsilon = \Delta\omega / \left[2\left(a - b\frac{C_{13}}{C_{33}} \right) \right], \tag{6}$$

where a and b are phonon deformation potentials, and C_{13} and C_{33} are elastic constants, respectively. The calculated values of stress and strain for different samples are given in Table 2. These data imply that the stress of the asymmetric pyramid has been significantly reduced in contrast to the planar LEDs, with a frequency shift range from 567.4 to 568 cm^{-1}. Even compared to the previous broadband emission microstructures (569.2 to 570 cm^{-1}) [19], which were grown on 2D patterned substrates by the traditional SAG method, our asymmetric pyramid growth on 3D patterned substrates still appears to be superior. It demonstrates that the deep-hole pattern is an effective method to reduce the residual stress. Additionally, we found that the lateral overgrowth region, including the LO wing and edge, has lower stress than the LO window. It shows that the lateral overgrowth can also contribute to stress relaxation.

To further investigate the influence mechanism of the residual stress on the radiative recombination rate, a theoretical calculation and a numerical analysis were performed based on the Raman test results. Since the spot size of the Raman test is far less than the dimension of each facet, the test results can be used to represent the residual stress of the specific plane. According to Fiorentini *et al.* [35], the spontaneous polarization (in C/m^2) of InGaN can be expressed to the second order in the composition parameter x as

$$P^{sp}_{In_xG_{1-x}N} = -0.042x - 0.034(1-x) + 0.038x(1-x). \tag{7}$$

For nitride nanostructures grown along the c axis and the strain imposed onto the epitaxial layer in the basal plane, the piezoelectric polarization can be expressed as a Vegard interpolation,

$$P^{pz}_{In_xG_{1-x}N} = xP^{pz}_{InN}[\varepsilon(x)] + (1-x)\,P^{pz}_{GaN}[\varepsilon(x)], \tag{8}$$

where the bulk piezoelectric polarization P^{pz}_{InN} and P^{pz}_{GaN} can be expressed accurately and compactly (in C/m^2) as

$$P^{pz}_{InN} = -1.373\varepsilon + 7.559\varepsilon^2, \tag{9}$$

$$P^{pz}_{GaN} = -0.918\varepsilon + 9.541\varepsilon^2, \tag{10}$$

as a function of the basal strain

$$\varepsilon(x) = \frac{\alpha_{basal} - \alpha(x)}{\alpha(x)}, \tag{11}$$

where α_{basal} is the basal GaN lattice constant and can be obtained using the residual stress ε calculated from the Raman result by $\alpha_{basal} = (\varepsilon + 1)\cdot\alpha_{GaN}$ and $\alpha(x)$ is the lattice constant of the unstrained alloy at composition x.

The built-in electric field in different strain conditions uses [36]

$$F^{InGaN} = \left| -\frac{P^{sp}_{InGaN} + P^{pz}_{InGaN} - P^{sp}_{GaN}}{\varepsilon_e^{InGaN}\varepsilon_0} \right|, \tag{12}$$

where F^{InGaN} denotes the built-in electric field of InGaN quantum well and ε_e^{InGaN} is the electronic dielectric constant of InGaN quantum well. The calculation results, which are listed in Table 2, demonstrate that the piezoelectric contribution dominates the polarization inside the QW because the spontaneous polarizations of GaN and InN do not noticeably differ. The residual stress strongly influences the piezoelectric polarization of QW. Thus, stress relief of the asymmetric (0001) facet due to the employment of the 3D substrate pattern and lateral overgrowth can effectively reduce the piezoelectric polarization of the MQWs, resulting in an effectively decreased built-in electric field.

This decreased built-in electric field can effectively improve the spontaneous emission rate, which can be proven by a numerical analysis using APSYS. Figures 6(a) and 6(b) show the calculated band diagrams of the LO asymmetric pyramid and planar LEDs at equilibrium and under a forward-bias condition. The basal lattice constant is set as 3.195 Å and 3.156 Å (1 Å = 0.1 nm) for the LO asymmetric pyramid and planar LED, respectively. Under the forward-bias condition, the

Table 2. Calculated Residual Stress, Polarization Field, and Built-in Electric Field Based on Raman Results

Sample Name	Raman Shift (cm^{-1})	Frequency Shift $\Delta\omega$ (cm^{-1})	Strain ε (%)	α_{basal} (Å)	x	P^{pz}_{InGaN} (C/m^2)	P^{sp}_{InGaN} (C/m^2)	P^{sp}_{GaN} (C/m^2)	F^{InGaN} (MV/cm)
ELO window–Point 6	568.0	0.77	−0.32	3.188	0.23	0.0349	−0.0291	−0.034	4.16
ELO wing–Point 7	567.4	0.22	−0.09	3.195	0.22	0.0299	−0.0292	−0.034	3.63
ELO edge–Point 8	567.5	0.33	−0.14	3.194	0.21	0.0353	−0.0294	−0.034	3.51
Reference	570.3	3.09	−1.28	3.156	0.18	0.0444	−0.0298	−0.034	5.07

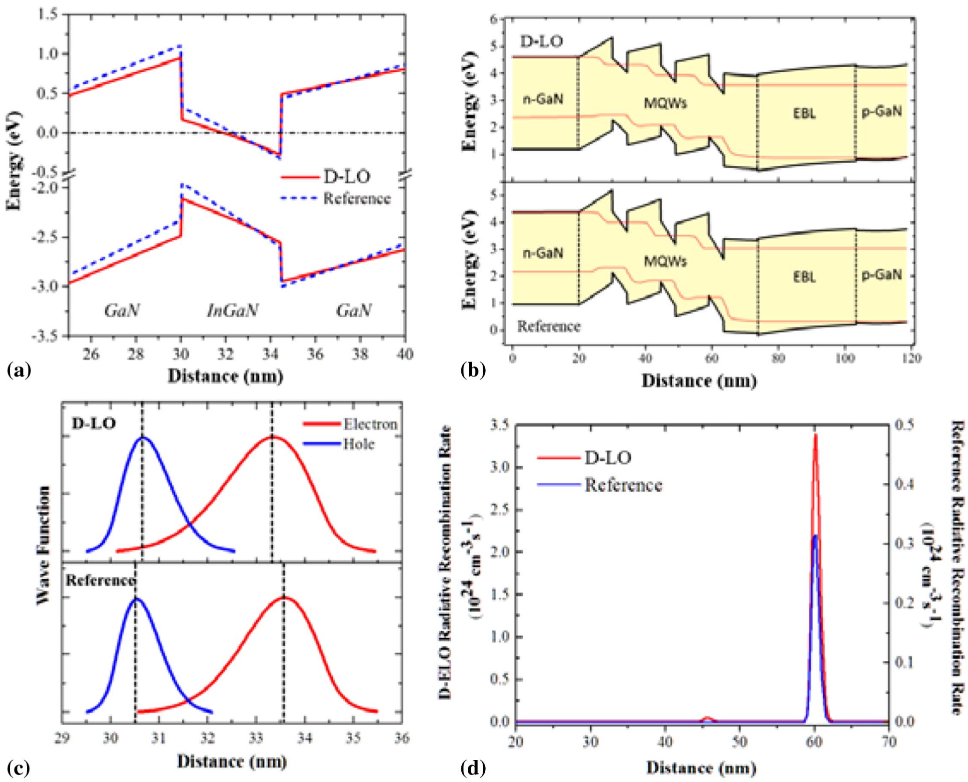

Fig. 6. Calculated energy band diagrams (a) at equilibrium and (b) under forward bias. (c) Electron and hole wave functions and (d) the radiative recombination rate of LO asymmetric pyramid and planar LED.

current density is 100 A/cm^2. The wave function of C1 and HH1 at equilibrium has also been calculated in Fig. 6(c). The band bending becomes less severe and the overlap of the electron and hole wave function is increased for the asymmetric pyramid, which demonstrates that the reduced residual stress can effectively lessen the built-in electric field. This reduced built-in electric field further contributes to an increased possibility for radiative recombination, lowering the carrier lifetime. The calculated radiative recombination rate of the asymmetric pyramid is 10 times that of the planar LEDs as a result, which is also consistent with the test results by TRPL. The numerical analysis demonstrates that the decreased built-in electric field due to the stress relief is the main reason for the enhancement of the radiative recombination rate and the reduction of the carrier lifetime.

Experimental and theoretical analyses demonstrate that stress relief due to the lateral overgrowth of the asymmetric pyramid can efficiently reduce the piezoelectric polarization and built-in electric filed, contributing to an increased possibility for a radiative recombination rate. This increased radiative recombination rate or reduced carrier lifetime is responsible for the enhancement of the modulation bandwidth.

4. CONCLUSION

In summary, we presented the fabrication of asymmetric pyramid microLEDs directly on the double-hole patterned sapphire substrate using laser drilling and SAG. Coalescence appears by reducing the hole distance and completely merged asymmetric pyramids are obtained by lateral overgrowth. Large-scale broadband emission appears for samples that have gone through the whole coalescence process, originating from the In segregation and QWs thickness variation at different locations via lateral overgrowth. The 3D substrate pattern and the lateral overgrowth also help reduce the strain and the dislocation density of the structure, resulting in an enhancement of the radiative recombination rate over a large emission range. As a result, the modulation bandwidth is significantly improved. This broadband high-speed emission makes an asymmetric pyramid viable for practical VLC applications.

Funding. Major State Basic Research Development Program of China (2016YFB0400801); National Natural Science Foundation of China (61774121, 6190030620); Natural Science Foundation of Shaanxi Province (2020JQ-074); Postdoctoral Research Foundation of China (2019M653640, 2019M663718); Fundamental Research Funds for the Central Universities (xjh012019038).

Acknowledgment. The SEM work was done at International Center for Dielectric Research (ICDR), Xi'an Jiaotong University. Dr. Zhenhuan Tian also thanks Dr. Jian Zhu for his help in life.

Disclosures. The authors declare no conflicts of interest.

REFERENCES

1. R. Wan, X. Gao, L. Wang, S. Zhang, X. Chen, Z. Liu, X. Yi, J. Wang, J. Li, W. Zhu, and J. Li, "Phosphor-free single chip GaN-based white light

emitting diodes with a moderate color rendering index and significantly enhanced communications bandwidth," Photon. Res. **8**, 1110–1117 (2020).
2. M. S. Islim, R. X. Ferreira, X. He, E. Xie, S. Videv, S. Viola, S. Watson, N. Bamiedakis, R. V. Penty, I. H. White, A. E. Kelly, E. Gu, H. Haas, and M. D. Dawson, "Towards 10 Gb/s orthogonal frequency division multiplexing-based visible light communication using a GaN violet micro-LED," Photon. Res. **5**, A35–A43 (2017).
3. S. Rajbhandari, J. J. D. McKendry, J. Herrnsdorf, H. Chun, G. Faulkner, H. Haas, I. M. Watson, D. O'Brien, and M. D. Dawson, "A review of gallium nitride LEDs for multi-gigabit-per-second visible light data communications," Semicond. Sci. Technol. **32**, 023001 (2017).
4. Z. Liu, C.-H. Lin, B.-R. Hyun, C.-W. Sher, Z. Lv, B. Luo, F. Jiang, T. Wu, C.-H. Ho, H.-C. Kuo, and J.-H. He, "Micro-light-emitting diodes with quantum dots in display technology," Light Sci. Appl. **9**, 83 (2020).
5. K. S. Kim, J. K. Son, S. N. Lee, Y. J. Sung, H. S. Paek, H. K. Kim, M. Y. Kim, K. H. Ha, H. Y. Ryu, O. H. Nam, T. Jang, and Y. J. Park, "Characteristics of long wavelength InGaN quantum well laser diodes," Appl. Phys. Lett. **92**, 101103 (2008).
6. S.-N. Lee, H. S. Paek, H. Kim, T. Jang, and Y. Park, "Monolithic InGaN-based white light-emitting diodes with blue, green, and amber emissions," Appl. Phys. Lett. **92**, 081107 (2008).
7. A. Rashidi, M. Monavarian, A. Aragon, A. Rishinaramangalam, and D. Feezell, "Nonpolar *m*-plane InGaN/GaN micro-scale light-emitting diode with 1.5 GHz modulation bandwidth," IEEE Electron Device Lett. **39**, 520–523 (2018).
8. W. Chen, G. Hu, J. Lin, J. Jiang, M. Liu, Y. Yang, G. Hu, Y. Lin, Z. Wu, Y. Liu, and B. Zhang, "High-performance, single-pyramid micro light-emitting diode with leakage current confinement layer," Appl. Phys. Express **8**, 032102 (2015).
9. S.-P. Chang, J.-R. Chang, K.-P. Sou, M.-C. Liu, Y.-J. Cheng, H.-C. Kuo, and C.-Y. Chang, "Electrically driven green, olivine, and amber color nanopyramid light emitting diodes," Opt. Express **21**, 23030–23035 (2013).
10. S.-W. H. Chen, C.-C. Shen, T. Wu, Z.-Y. Liao, L.-F. Chen, J.-R. Zhou, C.-F. Lee, C.-H. Lin, C.-C. Lin, C.-W. Sher, P.-T. Lee, A.-J. Tzou, Z. Chen, and H.-C. Kuo, "Full-color monolithic hybrid quantum dot nanoring micro light-emitting diodes with improved efficiency using atomic layer deposition and nonradiative resonant energy transfer," Photon. Res. **7**, 416–422 (2019).
11. J. Zhu, C. Lao, T. Chen, and J. Li, "3D-printed woodpile structure for integral imaging and invisibility cloaking," Mater. Des. **191**, 108618 (2020).
12. Y. Huang, G. Tan, F. Gou, M.-C. Li, S.-L. Lee, and S.-T. Wu, "Prospects and challenges of mini-LED and micro-LED displays," J. Soc. Inf. Disp. **27**, 387–401 (2019).
13. H. L. Minh, D. O. Brien, G. Faulkner, L. Zeng, K. Lee, D. Jung, Y. Oh, and E. T. Won, "100-Mb/s NRZ visible light communications using a postequalized white LED," IEEE Photon. Technol. Lett. **21**, 1063–1065 (2009).
14. J. Grubor, S. Randel, K.-D. Langer, and J. W. Walewski, "Broadband information broadcasting using LED-based interior lighting," J. Lightwave Technol. **26**, 3883–3892 (2008).
15. W. Feng, V. V. Kuryatkov, S. A. Nikishin, and M. Holtz, "Selective area epitaxy of InGaN quantum well triangular microrings with a single type of sidewall facets," J. Cryst. Growth **312**, 1717–1720 (2010).
16. M.-L. Lee, Y.-H. Yeh, S.-J. Tu, P. C. Chen, W.-C. Lai, and J.-K. Sheu, "White emission from non-planar InGaN/GaN MQW LEDs grown on GaN template with truncated hexagonal pyramids," Opt. Express **23**, A401–A412 (2015).
17. M. Funato, K. Hayashi, M. Ueda, Y. Kawakami, Y. Narukawa, and T. Mukai, "Emission color tunable light-emitting diodes composed of InGaN multifacet quantum wells," Appl. Phys. Lett. **93**, 021126 (2008).
18. Y.-H. Ko, J. Song, B. Leung, J. Han, and Y.-H. Cho, "Multi-color broadband visible light source via GaN hexagonal annular structure," Sci. Rep. **4**, 5514 (2014).
19. Y. C. Sim, S.-H. Lim, Y.-S. Yoo, M.-H. Jang, S. Choi, H.-S. Yeo, K. Y. Woo, S. Lee, H. G. Song, and Y.-H. Cho, "Three-dimensional GaN dodecagonal ring structures for highly efficient phosphor-free warm white light-emitting diodes," Nanoscale **10**, 4686–4695 (2018).
20. T. Wu, C.-W. Sher, Y. Lin, C.-F. Lee, S. Liang, Y. Lu, S.-W. H. Chen, W. Guo, H.-C. Kuo, and Z. Chen, "Mini-LED and micro-LED: promising candidates for the next generation display technology," Appl. Sci. **8**, 1557 (2018).
21. Z. Tian, Y. Li, X. Su, L. Feng, S. Wang, M. Zhang, W. Ding, Q. Li, Y. Zhang, M. Guo, F. Yun, and S. W. R. Lee, "Growth, characterization, and application of well-defined separated GaN-based pyramid array on micropatterned sapphire substrate," Appl. Phys. Express **10**, 092101 (2017).
22. H. Yu, L. K. Lee, T. Jung, and P. C. Ku, "Photoluminescence study of semipolar $\{10\bar{1}1\}$ InGaN/GaN multiple quantum wells grown by selective area epitaxy," Appl. Phys. Lett. **90**, 141906 (2007).
23. A. Chitnis, C. Chen, V. Adivarahan, M. Shatalov, E. Kuokstis, V. Mandavilli, J. Yang, and M. A. Khan, "Visible light-emitting diodes using *a*-plane GaN–InGaN multiple quantum wells over *r*-plane sapphire," Appl. Phys. Lett. **84**, 3663–3665 (2004).
24. W. Feng, V. V. Kuryatkov, A. Chandolu, D. Y. Song, M. Pandikunta, S. A. Nikishin, and M. Holtz, "Green light emission from InGaN multiple quantum wells grown on GaN pyramidal stripes using selective area epitaxy," J. Appl. Phys. **104**, 103530 (2008).
25. T. Tsuchiya, J. Shimizu, M. Shirai, and M. Aoki, "InGaAlAs selective-area growth on an InP substrate by metalorganic vapor-phase epitaxy," J. Cryst. Growth **276**, 439–445 (2005).
26. S. Hwang, N. Han, H. Jeong, J. H. Park, S.-H. Lim, J.-H. Cho, Y.-H. Cho, H. J. Jeong, M. S. Jeong, and J. K. Kim, "Optical and facet-dependent carrier recombination properties of hendecafacet InGaN/GaN microsized light emitters," Cryst. Growth Des. **17**, 3649–3655 (2017).
27. H. Kim, D.-S. Shin, H.-Y. Ryu, and J.-I. Shim, "Analysis of time-resolved photoluminescence of InGaN quantum wells using the carrier rate equation," Jpn. J. Appl. Phys. **49**, 112402 (2010).
28. L. Ferrari, J. S. T. Smalley, H. Qian, A. Tanaka, D. Lu, S. Dayeh, Y. Fainman, and Z. Liu, "Design and analysis of blue InGaN/GaN plasmonic led for high-speed, high-efficiency optical communications," ACS Photon. **5**, 3557–3564 (2018).
29. D. Lu, H. Qian, K. Wang, H. Shen, F. Wei, Y. Jiang, E. E. Fullerton, P. K. L. Yu, and Z. Liu, "Nanostructuring multilayer hyperbolic metamaterials for ultrafast and bright green InGaN quantum wells," Adv. Mater. **30**, 1706411 (2018).
30. H. Chun, S. Rajbhandari, G. Faulkner, D. Tsonev, E. Xie, J. J. D. McKendry, E. Gu, M. D. Dawson, D. C. O'Brien, and H. Haas, "LED based wavelength division multiplexed 10 Gb/s visible light communications," J. Lightwave Technol. **34**, 3047–8724 (2016).
31. T. S. Zheleva, W. M. Ashmawi, O.-H. Nam, and R. F. Davis, "Thermal mismatch stress relaxation via lateral epitaxy in selectively grown GaN structures," Appl. Phys. Lett. **74**, 2492–2494 (1999).
32. M. Kuball, M. Benyoucef, B. Beaumont, and P. Gibart, "Raman mapping of epitaxial lateral overgrown GaN: stress at the coalescence boundary," J. Appl. Phys. **90**, 3656–3658 (2001).
33. G. Nootz, A. Schulte, L. Chernyak, A. Osinsky, J. Jasinski, M. Benamara, and Z. Liliental-Weber, "Correlations between spatially resolved Raman shifts and dislocation density in GaN films," Appl. Phys. Lett. **80**, 1355–1357 (2002).
34. H. J. Chang, Y. P. Hsieh, T. T. Chen, Y. F. Chen, C. T. Liang, T. Y. Lin, S. C. Tseng, and L. C. Chen, "Strong luminescence from strain relaxed InGaN/GaN nanotips for highly efficient light emitters," Opt. Express **15**, 9357–9365 (2007).
35. V. Fiorentini, F. Bernardini, and O. Ambacher, "Evidence for nonlinear macroscopic polarization in III–V nitride alloy heterostructures," Appl. Phys. Lett. **80**, 1204–1206 (2002).
36. J.-J. Shi and Z.-Z. Gan, "Effects of piezoelectricity and spontaneous polarization on localized excitons in self-formed InGaN quantum dots," J. Appl. Phys. **94**, 407–415 (2003).